Retaining High Fracture Toughness in Aged Polymer Composite/Adhesive Joints through

Optimization of Plasma Surface Treatment

Nahal Aliheidari, Amir Ameli*

Department of Plastics Engineering, University of Massachusetts Lowell, 1 University Ave, Lowell, MA 01854, USA

* Corresponding author: amir_ameli@uml.edu

Abstract

A response surface methodology was used to analyze the flow rate, power, and time factors of plasma surface treatment. Surface free energy (SFE) of treated glass fiber-reinforced composites showed a strong quadratic dependence on flow rate, power, and time, with significant interaction between time and power. Optimized factors predicted a maximum SFE of 78.63 mN/m, which matched well with the measured value of 77.42 mN/m, accounting for 2.46 times increase in SFE against untreated case. Moreover, with plasma treatment, the SFE's polar component became dominant (99%) as also confirmed with FTIR spectroscopy. Fracture toughness testing of fresh and aged adhesive joints proved a more stable interface for plasma-treated specimens due to the covalent bonds facilitated by the functional groups formed during the treatment. Consequently, the fracture toughness of the plasma-treated specimens did not drop after seawater immersion, while that for the untreated and sand-treated specimens showed about a 15% drop.

Keywords: Plasma surface treatment, Hydrothermal aging, Fracture toughness, Response surface methodology

Introduction

Due to their high strength-to-weight ratio, stiffness, and durability, glass fiber-reinforced polymer (GFRP) composites have found wide application in various manufacturing industries, including aerospace [1,2], marine [3], civil structures [4], and wind turbine blades [5]. During their expected service life of decades, these components may be exposed to harsh environments and versatile loading conditions. In the form of the final

structure, these parts are usually joined with some other components such as other GFRP, aluminum, or stainless-steel elements using structural adhesives.

The adhesive bonding method has been a great alternative to conventional joint fabrication techniques such as welding and mechanical fastening due to the reduction in stress concentration points, better fatigue performance, corrosion resistance, vibration damping, and the high strength-to-weight ratio [6]. Thanks to the enhanced chemistry, the method can also be successfully applied to dissimilar materials which is another predominance over the conventional techniques [7].

The surface preparation of GFRP components is a critical step where the success or failure of the adhesively bonded joint is heavily affected. The final performance and properties of the adhesively bonded joints depend significantly on the quality of the interface formed between the two substrates [8–10]. Therefore, the major purpose of surface preparation is to produce a contaminant-free surface and increase its free energy so that a stronger bonding can be formed [11].

Figure 1 presents various surface treatment methods that can be used to improve GFRP's surface before bonding. The methods are divided into mechanical, chemical, and physico-chemical treatments [12,13]. The ultimate goal of employing each of these methods is to remove contaminants such as dust and lubricant from the surface, enhance the surface wettability and surface free energy to produce a more active surface for better adhesion. Therefore, a proper selection of the surface treatment method is vital for bond quality.

[Figure 1 about here.]

Peel ply is one of the most common methods that is used to protect the surface. Peel ply is a sacrificial layer that is applied to the surface of the composite before curing. Removing the peel ply should generate a clean and rough surface. However, the interaction of matrix resin with peel ply, and the peel ply residue affects the joint strength such that the resultant joint strength is lower, compared to the other mechanical surface treatment methods [14].

Another common method is using abrasive materials such as sandpaper on the composite's surface to remove the unwanted layer and generate a rough surface. The method is simple and cost-effective, and it can

produce different surface roughness values based on the sandpaper grit number. However, it is highly likely to damage the underlying reinforcing fibers during any surface roughening using sanding or sandblasting [15]. Further, The composite substrate's properties may significantly deteriorate through sandblasting, as it removes a substantial amount of the resin layer from the surface [16].

Solvent wiping is the easiest chemical method to clean the surface. It should however be used properly.

Otherwise, the solvent's residue can interfere with the adhesive and affect the final joint properties [17]. UV curing, a process that involves the light-triggered polymerization of multifunctional oligomers, has also been investigated as a surface treatment. This method is primarily used on thermoplastic materials [18]. The adhesion of UV coatings is often compromised due to the low surface free energy of polymer substrates and shrinkage [19]. Primers are also usually used for thermoplastic materials, and it is not a suitable treatment process for thermosets in GRFP composites.

Plasma treatment (Figure 2) is one of the most efficient methods for polymers' surface treatment [20,21].

Decent bonding properties, long-term durability, not affecting the bulk properties of the substrate, and not being abrasive are a few advantages of plasma treatment [22].

[Figure 2 about here.]

One notable characteristic of plasma treatment is its ability to interact with a surface through physical, chemical means, or a combination of both, depending on the specific factors selected for the treatment process [23]. The physical alteration of the material surface is attributed to ions, whereas free radicals induce chemical modifications. Plasma is a complex phenomenon involving a combination of excited electrons, atoms, molecules, and radical species generated when a gas is subjected to an electric field. The selection of the gas used also plays a crucial role in determining the resulting surface properties. For instance, argon and neon are typically employed for cleaning purposes, oxygen for increasing hydrophilicity, and fluoride for promoting hydrophobicity [22].

Plasma surface preparation has been extensively utilized in the treatment of various thermoplastic materials, including but not limited to polyesters, polyether ether ketone (PEEK), polyethylene, polylactic acid, polydimethylsiloxane (PDMS), polyamide (PA), and polypropylene (PP) [24–28]. More recently, this method

has been employed to improve the adhesion between fillers - such as carbon fiber - and polymeric matrix, through the modification of the filler surface properties. [29–31]. Brooj et al. [32] optimized the plasma treatment factors for carbon fiber surface treatment using a Box Behnken design and investigated how the fiber surface treatment affects surface topography and fiber/matrix adhesion. Several studies have reported that using non-optimized plasma factors can lead to a decline in adhesion properties and interlaminar shear strength in adhesively bonded joints where woven carbon fibers were plasma-treated prior to impregnation [33]. There are some reports that utilized the one-factor-at-a-time design of experiments to investigate the impact of plasma process factors on carbon fibers [34]. Haji et al. investigated the effect of plasma treatment on the tensile strength of GFRP/epoxy composite. In their study, the GF mat was treated with oxygen plasma and impregnated with an epoxy resin and hardener mixture [35].

However, there is limited research on the use of plasma for surface modification of thermoset polymers in fiber-reinforced composites [36]. Gude et al. [37] conducted a study on the surface properties of carbon fiber/epoxy laminates (substrate) with different surface treatments including plasma to correlate the surface morphology and mechanical properties. They reported that chemical composition and mechanical interlocking are the dominant mechanisms in lap shear and fracture tests, respectively [37]. Very recently, Wang et al. [38] researched employing two surface preparation methods including peel ply and plasma treatment on the fracture toughness of carbon fiber-reinforced polymer (CFRP)/epoxy adhesive joints. The study comprehensively considers the phenomena behind the observations, however, only time was considered as the process factor. To the best of the author's knowledge, there is no systematic study to investigate the correlations between the plasma process factors and the surface wettability (i.e., the contact angle and surface free energy) of GFRP composites.

The objective of this study was to understand and quantify the relations between the plasma treatment factors and the surface wettability of GFRP composites and employ the developed statistical models to optimize the treatment process. A central composite response surface design of experiment was planned and executed to establish quadratic models. The surface characterizations included the measurements of the contact angle, surface free energy, and surface roughness. The statistical quadratic model was used for the process optimization and the predictions at the optimized process conditions were verified against the experimentally measured

surface free energies. The superior performance of the plasma treatment especially in maintaining high fracture toughness after aging was discussed in detail against the untreated and sand-treated surfaces and the differences in the underlying mechanisms were also identified.

2. Experimental procedures

2.1. Materials

A commercial G-10 FR-4 woven glass fabric/epoxy laminate with low water absorption coefficient was used as the substrate. The GFRP had a glass transition temperature of about 130 °C and a density of 1,800 kg/m³. EPIKOTETM resin MGS® BPR 135G3 with EPIKURETM curing agent MGS® BPH 137GF with the required volumetric mixing ratio of 2:1 was used as the adhesive system, which was provided by Westlake Epoxy.

2.2. Surface treatment

Two different surface treatments, namely cold radiofrequency plasma treatment, and rotary sanding were employed to modify the GFRP surface.

2.2.1. Plasma treatment

The plasma surface treatment was performed using a PE-100 Benchtop Plasma System (Plasma Etch, USA) under vacuum conditions. The machine was equipped with a 300W, 100KHz continuously variable power supply. The chamber was designed with three stacked horizontal electrodes with 23×33 cm² and 8 cm clearance. The plasma treatment was conducted using Oxygen (O₂) as the carrier gas with a purity of 99.5%. The chamber pressure was maintained at 0.2 Torr during the treatment.

A design of experiment (DOE) was employed using the central composite design (CCD), which is a type of response surface methodology (RSM). RSM is a statistical method for design of experiment and developing mathematical models that can incorporate the main effects in linear and high-order terms as well as their interactions [39]. Further, RSM is the most common methods to optimize process factors with a single response [40,41]. Compared to full factorial designs (FFD), RSM offers the benefit of fewer numbers of runs and the capability to assess the higher-order terms (e.g., quadratic), which is not possible with the other methods [42]. The central composite design (CCD) is a frequently used method for creating second-order response models

among several response surface methodologies (RSMs). The second-order polynomial regression equation used for modeling the response is given by:

$$y = \beta_0 + \sum_{i=1}^k \beta_i x_i + \sum_{i=1}^k \beta_{ii} x_i^2 + \sum_{i < j} \sum_{j=1}^k \beta_{ij} x_i x_j + \epsilon$$
 (1)

where y is the response, x is the design factor, β is the regression coefficient, k is the number of design factors, and ϵ is the error term [43].

The CCD here was planned in two blocks and three plasma process factors were identified through an initial screening process, namely time (s), power (W), and flow rate (ccm), in five levels each. Surface free energy was considered the main response in the DOE. The input process factors and their levels are tabulated in Table 1. The range of each process factor was selected based on the machine's capability and performing a few screening experiments.

[Table 1 about here.]

Minitab statistical software Version 21.1.0 was used in building the DOE and conducting the statistical analyses. The CCD design was built with 5 levels of each factor and randomized by the software. Table 2 lists the total of 20 experimental runs in randomized order including the coded and actual levels of each factor and the corresponding SFE response.

[Table 2 about here.]

2.2.2. Sanding treatment

The surface sanding with different grit numbers (80, 200, 400, 600, 800, and 1200) was conducted to create mechanical abrasion using a rotary sanding machine (Bosch orbit sander, GEX 125-1 AE). The sanded surface was cleaned with compressed air followed by acetone wiping. The samples were then left to be air-dried for 48 hours before any further measurements.

2.3. Surface characterization

2.3.1. Contact-angle measurement and estimation of surface free energy

Ionized water, glycerol, and ethylene glycol were used to measure the contact angle using an optical tensiometer (Biolin Scientific Theta Flex, USA) by the sessile drop technique. To minimize the time effect between the plasma treatment and contact angle measurement, all the contact angle measurements were conducted within 15 min of the plasma treatment. Three composite samples were tested for the contact angle measurement of each liquid. An automatic dispenser placed 10 drops of each liquid (a total of 30 drops) on the surface of each composite sample. The images of each drop were captured by the machine after they reached the steady state and then analyzed using OneAttention software to obtain the contact angle of each drop. For each composite/liquid combination, the average of the ten measured contact angles was used. For three composite sample replications, the mean and standard deviations are calculated and reported.

The measured contact angles were used to estimate the free surface energy by OneAttention software. There are various methods to obtain the surface free energy (SFE) including Young's equation, Fowkes & Extended Fowkes, Zisman model, Owens-Wendt-Rabel & Kaelble model, etc. [44–46]. The model selection should be done based on the surface properties and polarity. In particular, Fowkes model can determine the polar and dispersive components of SFE. A development of the Fowkes approach is the OWRK/Fowkes model which can better estimate the polar and dispersive components using multiple liquids with different surface energies. The OWRK/Fowkes model was then used here together with three liquids to calculate the SFE. which is an approach that applies geometric mean to combine the polar and dispersive components according to Eq (2) [47]:

$$\sqrt{\gamma_s^d \gamma_l^d} + \sqrt{\gamma_s^p \gamma_l^p} = 0.5 \gamma_i (1 + \cos\theta) \qquad (2)$$

 γ_s and γ_l are the surface free energies of solid and liquid with gas interface, respectively. Superscripts d and p correspond to the dispersive and polar components, respectively. θ is the measured contact angle (°) between the solid and the liquid. The only two unknowns in this equation are γ_s^d and γ_s^p and at least two liquids are needed to obtain these values. The total SFE of the composite surface is γ_s , which is equal to the sum of γ_s^d and γ_s^p . Table 3 lists the polar, dispersive, and total surface energy components for the three liquids that were used for the SFE measurements and calculations here.

[Table 3 about here.]

2.3.2. Fourier transformed infrared spectroscopy

To investigate the chemical bonds and composition of the GFRP before and after surface treatment, Fourier-transformed infrared spectroscopy was performed in attenuated total multiple reflection mode. The samples were cut in 10*10*1mm³. The spectroscopy was conducted by Nicolet 4700 (Thermo Nicolet Nexus, USA) using a diamond prism and 32 scans. The graphs were analyzed using peak spectroscopy software.

2.3.3. Surface roughness

The surface topography of the untreated, plasma-treated, and sanded GFRP composite samples was analyzed using an optical profilometer (Wyko NT 2000, Veeco, USA). $1.2\times0.9~\text{mm}^2$ area of each sample was scanned and at least three replications were performed for each condition. The surface parameters (S_a , S_q , and S_z values) were calculated using Gwyddion software where S_a , S_q , and S_z are the mean roughness, root mean square roughness, and the mean of the height difference between the highest peaks and the lowest valleys. The untreated sample was cleaned with cheesecloth, the plasma samples were treated at 64 s, 118 W, and 36 ccm of time, power, and flow rate, respectively, and the sanded samples were prepared with 800 grit sandpaper.

2.3.4. Scanning electron microscopy

The samples treated under different conditions were subjected to scanning electron microscopy (SEM) to observe the surface variations. The samples were gold sputtered with Denton Vacuum Desk IV sputter coater and imaged using JEOL 6390 SEM (Jeol USA Inc).

2.4. Joint fabrication, hygrothermal aging, and fracture testing

For hygrothermal aging of the joints, open-faced specimens were made by joining only one GFRP substrate to the adhesive layer [48]. The resin and the hardener were first mixed using a speed mixer (Speed Mixer, DAC 400.2 VAC-P FlackTek Inc) at two steps of 2 min at 850 rpm followed by another 2 min at 1000 rpm under the vacuum. The mixed adhesive system was then applied on the treated surfaces of the GFRP substrate within 15 min of the surface treatment. The precrack was created by embedding a PTFE film of 25 µm thickness and 75 mm length within the adhesive layer. The primary adhesive layer had a thickness of 1.05 mm, which was controlled using metallic spacers. After completion of the adhesive layer application and placing the precrack, the adhesive layer was covered by a high-temperature release film and the stacking was completed by adding a metallic backing plate on top of the release film. The assembly was then placed inside an automatic compression

molding system where the temperature of the adhesive joint assembly was programmed and controlled according to the recommended cure cycle (6 hours at 65°C followed by 2 hours at 85°C). A pressure profile was also developed and maintained during the curing cycle to assure the uniformity and consistency of the adhesive layer thickness. The assembly was then cooled down to room temperature and the backing plate and the release film were removed, making the open-faced specimen ready. The open-faced specimen was then immersed in seawater with a salinity of 35% at 65°C [49] for one week followed by drying at 40°C for 5 days. The open-faced specimen was closed by bonding the aged open-faced specimen with a secondary adherend using a secondary layer of adhesive (0.15 mm thickness) [48] using the same curing procedure.

The mode II fracture parameters were determined using ENF specimens. The ENF specimen was made based on modified ASTM D7905. The final joint was prepared by closing the dried specimens with an unaged GFRP substrate using the secondary adhesive layer (thin layer with a thickness of 0.15 mm). Figure 3(a) gives a photograph of a completed open-faced joint and Figure 3(b) provides a schematic of the joint illustrating different parts and the loading conditions. The closed joints had the same geometry, dimensions, and curing history, except the aged layer was replaced with the fresh unaged layer of adhesive. The total adhesive thickness was also the same for both aged and unaged cases.

[Figure 3 about here.]

This resulted in a complete end-notched flexural (ENF) fracture specimen, according to ASTM D7905M. The ENF specimens were then loaded using a 10 kN universal testing machine (Instron 5960, USA) with 0.5 mm/min of crosshead displacement rate and the load-displacement data were recorded (Figure 3(c)). The critical mode II fracture toughness (G_{IIC}) was then calculated based on the modified beam theory [50] as follows:

$$G_{IIC} = \frac{3mP_{max}^2 a_0^2}{2B} \tag{3}$$

where m presents the compliance calibration coefficient obtained from linear regression analysis of the compliance versus crack length graph, P_{max} , a_0 and B are the maximum load, crack length used in the fracture experiment (30 mm) and specimen width, respectively. Unaged fresh joints, having identical dimensions to those of aged one, were also made and tested to obtain the fracture toughness of fresh joints.

3. Results and discussion

3.1. Statistical analysis

3.1.1. Response normality

The full quadratic model was used for the statistical analysis to correlate the response to the factors and their interactions on the model and consider the prediction accuracy. The full quadratic equation is obtained as follows:

$$SFE = 77.60 + 1.76T - 0.15P + 3.85F - 3.87T^{2} - 3.07P^{2} - 4.39F^{2} + 1.85T \cdot P + 0.80T \cdot F + 0.57P \cdot F$$
(4)

The initial step involved examining a normal probability plot of the standardized residuals, in order to ensure that the fitted model provided an accurate representation of the underlying system. As illustrated in Figure 4 (a), the close alignment between the observed distribution of residuals and the anticipated distribution suggests that the error terms had a normal distribution, indicating that the model approximated the actual system effectively. To further check the adequacy of the model and assurance of the normal distribution, the histogram, and the quantile-quantile (Q-Q) plot were assessed. The histogram (Figure 4b) exhibited a normal distribution with an acceptable approximation. Q-Q plot tends to be more sensitive in identifying long tails or outlying data points. As shown in Figure 4c, no systematic departures from the straight line in the Q-Q plot were observed, which is another proof that the data is normally distributed.

Once the normality assumption of the model was confirmed, the significance of the factors was assessed. Figure 5 shows the Pareto chart of the standardized effect of each main factor, quadratic terms, and two-way interactions from the CCD analysis without any transformation function. The reference line for the statistical significance depends on the significance level which was assumed α =0.05 in this study.

[Figure 5 about here.]

3.1.2. Regression model and significant terms

It should be noted that the factors or interactions having a value smaller than the reference line (Figure 5) do not have any significant effect on the model with a confidence level of 95%. Since this DOE model will serve as

the predictive model used by the data mining algorithm to predict new or future observations [51], to increase the robustness of the proposed model and decrease the cost, insignificant interactions will need to be removed from the model before further processing. The interactions (T*F and T*P) were found insignificant and thus removed carefully from the model through step-by-step model simplification to check whether a simpler reduced model can be proposed. However, the main factor P could not be removed due to the hierarchy requirements since its quadratic term and interactions are significant.

The statistical values of the Analysis of Variance (ANOVA) for factors T, P, and F, including their quadratic terms and two-way interactions, are presented in Table 4. It is important to note that any term with a p-value less than 0.05 is considered significant in the output response at a 95% confidence level. The Sum of Squares (SS) value reflects the impact of a factor on the deviation of the response from its grand mean; hence, a factor with a high SS value indicates a strong influence on the response. Based on the SS, F-values, and p-values (Table 4), the significance of the terms is square > linear > interactions. Within the square terms, the order of significance is time > power > flow rate.

[Table 4 about here.]

The p-value of the lack-of-fit was 0.57 which means it is not significant while that for the model was 0.00001 (very small), indicating that the model fits the RSM data significantly. The coefficient of determination (R^2) and the adjusted (adj- R^2) were 95.59 and 92.07%, respectively. An R^2 value of 95.59% indicates that 95.59% of the response behavior is explainable by the proposed model. A value above 80% for R^2 is necessary for a good fitness of the model, while a higher R^2 value indicates a great accordance between the experimental data and data estimated by the model [52,53].

The regression equation of the refined model is given below in terms of the uncoded values of the process factors:

$$SFE = 77.60 + 1.76T - 0.16P + 3.85F - 3.87T^2 - 3.07P^2 - 4.39F^2 + 1.85T \cdot P$$
 (5)

where, a positive sign and a negative sign of a term coefficient indicate synergistic effect and antagonistic effect [54], respectively. For the first-degree (linear) terms, time and flow rate were positive implying that these factors have a positive correlation with SFE response. The coefficient of the quadratic terms was, however,

negative for all three factors. Further, p-value is considered significant when it is less than the selected significance level (α =0.05 in this case), indicating a statistically significant relationship between the predictor and the response. Additionally, the Variance Inflation Factor (VIF) was used to examine multicollinearity. VIF measures the extent to which the variance of a given regression coefficient increases when the predictors are correlated. A VIF of 1 indicates no multicollinearity, but as it deviates from 1, the correlation between the predictors increases [55]. It is noted that the VIF values less than 3 and close to 1 are commonly used as a rule of thumb for indication of no concern in the model and problematic collinearity, respectively [56,57]. The VIF values here for all the model terms are between 1 and 1.27, suggesting that there is no substantial multicollinearity of the factors in the model.

In terms of the linear interactions, time*flow rate interaction was removed from the regression equation since it was not significant. That means the effect of time and flow rate on SFE were independent of each other, such that the amount of time duration does not alter the effect of flow rate on SFE. The same analysis holds true for the power*flow rate. However, the significant positive interaction effect between two factors of time and power means the increase of one factor (e.g., time) will elevate the effect of the other (i.e., power).

Further, the significance of the quadratic terms implies that the relationship between the process factors and the response is nonlinear. Since the first-order terms (time and power) are positive and their second-order terms (time² and flow rate²) are negative, the response surface can be parabolic with a maximum. It will be explained further in the following section.

3.2. Plasma treatment optimization using RSM

Before optimization, the main effects of process factors and their interactions were investigated by analyzing the factorial plots. Figure 6 (a) shows the main effect plots for time, power, and flow rate, and the higher the slope, the greater the effect of the factor [58]. While the flow rate has the most significant effect, it should be noted that all three main factor curves exhibit positive and negative derivatives, which indicate the importance of optimization for the plasma treatment.

The chemical structure of epoxy provides several side segments through which the structure can be oxidized without the scission of the macromolecular network for a short period of time, resulting in an increase in the

SFE. However, as the process factors increase excessively, chain scission may occur through both volatilization and surface degradation. Reducing the SFE suggests a modification or reorganization of the oxidized groups that play a role in the polar characteristic of the treated surface [59]. The phenomenon could be further explained with the degradation model of the epoxy surface, provided by Lim et al. [60], which shows that with excessive plasma exposure, the bonds are destroyed, leading to serial destruction toward the inside from the surface. The destructed chains rebound with oxygen, and finally, an electrical double layer on the surface would be formed. This observation aligns with Wang et al.'s report [38] which shows that the extension of treatment time can change the effectiveness of the treatment.

[Figure 6 about here.]

In the interaction plots, as interaction becomes weaker, the effect curves tend to be more parallel to one another [61]. Figure 6 (b) illustrates the significance of the time and power terms' interaction as the curves intersect one another. It should be noted that the other two interactions were insignificant and thus removed from the model and not reported in Figur Figure 6 (b).

The 2D contour plots of the SFE as a function of power/time, flow rate/time, and flow rate/power are also depicted in Figure 7. 2D contour plots provide visual guides that can be used in the process of factor selections for a certain range of targeted responses. It is seen that the SFE response peaks at the mid-range of all the process factors combinations. The red ovals in 7 (a)-(c) all correspond to an SFE value of greater than 75 mN/m while moving to both the high and low extremes, blue contours appear which indicate SFE values less than 55 mN/m. It is noted that the minimum coded value of Power factor in Figures Figure 6 and 7 is -1.0, instead of -1.63, as the plasma treametn was not able to provide a consistent process at the lowest level of power and the response was excluded (run No. 16 in Table 2).

[Figure 7 about here.]

The process optimization was performed through Response Surface Optimization (RSO) technique, which is a setting of factorial input values, such that the response reaches a desired level. The software provides the optimum condition based on the desirability function approach. The approach was developed by Harrington and later modified by Derringer and Suich [62]. Here, surface modification aims to activate the functional groups and

increase the surface energy. Therefore, the optimization objective was to maximize the value of SFE, which ideally corresponds to a desirability value of 1.0. The factors and the solution desirability values are calculated and tabulated in Table 5 for three solutions. The closer the predicted response is to the target requirements, the closer the desirability will be to 1.0. Therefore, solution one provides about 90% desirability which is close to 1.0 and seems to provide a favorable result. The reason that the optimization solution cannot reach a desirability value of exactly 1.0 is related to the "within sample" variation at the Central Point which sets 81.27 mN/m as the maximum value. It is however noted that the mean response at the Central Point (run numbers 1, 3, 4, 7, 15 and 20 in Table 2) is 78.48 (with 3.32 of standard deviation), which is very close to the maximum prediction with the highest desirability.

[Table 5 about here.]

To estimate the accuracy of the model prediction, the optimization solutions were tested by performing plasma treatment on the substrate with predicted factors and measuring SFE. The experimental SFE values for solutions 1, 2, and 3 were measured to be 77.42, 72.80, and 73.52, respectively. The maximum difference between the optimization results and measured SFE values is only 3%, indicating a good agreement between the prediction and the measurements. It is also worth noting that the maximum SFE can be reached in slightly over a minute, indicating that the treatment process is relatively fast.

3. Comparison to untreated and sand-treated surfaces

Figure 8 presents the SFE for the GRFP composite samples sanded with different grit numbers. It was observed that the SFE value of the untreated sample decreased once it was sanded using the smallest grit number of 80, which provides the roughest surface. With an increase in the grit number from 80 to 800, the SFE increased approximately linearly from about 20 to 44 mN/m. Further increase of the sanding fineness by using a grit number of 1200 caused a reduction in the SFE again to about 20 mN/m, which is comparable to that of the untreated sample. A similar trend of SFE with grit number was also reported by Yang et al. [63].

[Figure 8 about here.]

It is also interesting to note that the SFE's polar component, γ_s^p was found to be significantly smaller than its dispersive component, γ_s^d , specifically, for the cases of 600 and 800 grit numbers that provided the largest SFE

values. This may be attributed to the fact that the governing mechanism of sand treatment to improve the surface energy is merely physical by manipulating the surface topology. Once the sanding process is at its optimum condition, the SFE has merely a dispersive component. When sanding continued with a finer grit number (1200), the SFE decreased, and the energy components were similar to those of the untreated sample. The finer the grit, the less change on the surface topology. Since the 800 grit case provided the highest total SFE, this condition was considered for the rest of the study.

Figure 9 (a) and (b) show the contact angle and SFE, respectively, of the untreated, sanded (800 grit), and plasma-treated (optimized condition) samples. The water contact angle for untreated and sanded samples were 83.4, and 92.9, respectively, and then dropped to 35.8 after plasma treatment which is due to the raise in the surface polarity. Comparing the untreated and sanded samples, the sanded samples exhibited more wettability when exposed to ethylene glycol, but slightly higher contact angles when it was in contact with water and glycerol. Overall, the plasma-treated samples showed the lowest contact angles with all three liquids. This is attributed to the creation of active functional groups such as alkoxy, carbonyl, and carboxyl groups on the GFRP surface, and dipole-dipole attraction which resulted in enhanced surface wettability.

[Figure 9 about here.]

The SFE is divided into polar and dispersive components. Dispersive forces are very weak forces between all molecules, regardless of the structure or composition of the molecules, whereas the polar surface energy results from the attraction of charges between molecules. As seen in Figure 9 b, overall, both sanding and plasma surface treatment increased the SFE by about 39% and 157%, respectively. The surface free energies of the sanded and plasma-treated samples exhibited two significant differences. Firstly, the plasma-treated samples displayed a total SFE that was 85% higher than that of the sanded samples. This finding aligns with the adhesion theory which suggests that a stronger bonding force is generated by a higher surface free energy of the specimens [63]. The second difference was the type of forces that generate surface energy. It is very interesting to note that the surface energy of the plasma-treated sample was predominantly polar, forming about 99% of the total SFE. However, the sanded samples exhibited primarily dispersive components. In sanding treatment, the surface is modified by removing weak boundary layers and contaminants, and the surface characteristics including morphology, composition, and roughness are changed. Furthermore, since sanding is only a

mechanical process, no new active surface composition may be formed. Conversely, in plasma treatment, a shallow plasma layer having reactive species is deposited onto the target surface. The plasma causes ablation, which cleans the surface by eliminating the low molecular weight organic contaminants, and activates the surface by replacing surface atoms with more reactive chemical groups [64]. According to the SFE results, plasma treatment appears to be a more effective method for enhancing the substrate surface's wettability, making it more beneficial for subsequent surface processing such as adhesive bonding and coating.

FTIR analysis was employed to identify the changes that occur in the GFRP's molecular structure upon surface treatment and observe the appearance of new functional groups or disappearances of existing ones.

FTIR-ATR spectra of neat, sanded, and plasma-treated samples are presented in Figure 10. The broad band at 3200-3500 cm⁻¹ is attributed to the O-H stretch. The absorption peaks between 2800–3000 cm⁻¹ (-CH stretching) correspond to -CH₂- and -CH₃ which are stable methyl groups in the backbone of the polymer. These groups usually are not sensitive to curing and heat treatment [65]. The bands recorded at 1234 cm⁻¹ is attributed to C-O-C, and 937, and 832 cm⁻¹ absorption bands confirm the presence of free oxirane ring from the epoxy units [66,67].

[Figure 10 about here.]

It should be noted that the O-H peak was attenuated after sanding treatment. That can be due to the removal of the epoxy from the outer layer and exposure of more glass fibers. On the other hand, the intensity of the O-H band was increased by plasma treatment, which could be an indication of forming more O-H bands during treatment with oxygen plasma [68,69]. Plasma treatment can also result in the formation of carbonyl groups on the substrate surface [70]. This was observed by a significant increase in the intensity at 1745 cm⁻¹, which is a characteristic of stretching vibrations of C=O bonds. This is an indication of surface oxidation and hydrophilization using oxygen plasma [69].

As it can be seen in Figure 10, plasma treatment also modified the aliphatic carbon-hydrogen (C-H) bonds in the epoxy substrate. This results in changes in the intensity of peaks in the range of 2850-3000 cm⁻¹, which are associated with stretching vibrations of C-H bonds. Further, after plasma treatment, the functional surface group of O-C=O is also formed. This functional group reacts with hydrogen in the adhesive during the joint fabrication

process and forms the carboxyl chemical bonds. This bond significantly affects the stress transfer between the substrate and adhesive layer and thus enhancing the interfacial adhesion [71].

Figure 11 shows the surface topography of untreated, sanded, and plasma-treated GFRP samples. Table 6 also lists the surface roughness values. The average values of the surface roughness (Table 6, Sa) are 0.896±0.054, 0.424±0.067, and 0.892±0.015 µm for untreated, sanded, and plasma-treated samples, respectively. Sanding decreased the surface roughness significantly (~53%) by removing the taller peaks on the surface. However, the surface topology (Figure 11) and roughness (Table 6) of the untreated and plasma-treated samples were found to be very similar, indicating that the SFE could be significantly enhanced by an optimized plasma treatment without significantly altering the surface topology. As the dispersive component is attributed to the topological features, the observations of Figure 11 is also in line with the SFE polar and dispersive components (Figure 9) where plasma treatment did not yield any significant dispersive component. It should be noted that plasma-induced topological changes are minimal only if the treatment is optimized. It has been reported that if plasma treatment continues for longer times, the physical attributes of the surface also start to change significantly [72].

[Figure 11 about here.]

[Table 6 about here.]

Figure 12 illustrates the SEM micrographs of the GFRP surfaces. For the untreated sample, the results showed an overall smooth surface with occasional pores and scratches due to manufacturing and handling defects. In the sanded specimen (Figure 12b), the long lines are visible on the epoxy matrix, due to the rotary sanding operation. Another general and dominant feature observed on the sanded surface was debris from the resin residues together with some exposed and scratched glass fibers. Similar to the topology scans in Figure 11, the SEM morphologies also revealed significant similarities between untreated and plasma-treated surfaces, indicating a minimal physical change on the surface after plasma treatment.

[Figure 12 about here.]

Figure 13 depicts the upper side adherend's fracture surface of the aged ENF specimens with different surface treatments. In all the case, a small continuous strip of the adhesive was observed on this adherend side, indicating that the beginning of crack propagation occurred by shear cohesive failure from the crack tip, which was fully embedded within the adhesive layer [73]. In the untreated and sanded specimens, the crack quickly moved toward the interface between the GFRP and the adhesive layer promoting a mixed adhesive/cohesive failure mode. This is evident from Figure 13 (a) and (b) where the substrate's glass fiber imprints are visible next to the patches of adhesive. For the plasma-treated specimens, however, it was found that all the surface area was covered with a rough adhesive layer (Figure 13 (c)), which indicates that the failure mainly occurred cohesively inside the adhesive layer.

[Figure 13 about here.]

Figure 14(a) shows the load-displacement curves of fresh and aged fracture specimens prepared with untreated, sand-treated, and plasma-treated substrates. The overall shape of the curves was similar for all the specimens, indicating that the crack stability and ductility characteristics of the failure was similar for all the conditions. It should be noted that the peak loads and compliance cannot be directly compared amongst various conditions in this figure, as the differences in the substrate width and thickness from one condition to another can also cause a difference in the peak load and the compliance. The ASTM D7905 Non-Precracked (NPC) Compliance Calibration method was conducted for each individual specimen by three times of loading at different precrack length to obtain the experimental compliance coefficient (m) which was used together with the peak load and specimen geometry to calculate the *G_{IIC}* for each specimen.

Figure 14(b) shows the G_{IIC} of untreated, sanded, and plasma-treated joints tested at fresh and aged states. In both fresh and aged states, sanding did not appear to have any significant advantage over no treatment. The plasma treatment caused some improvement on the fracture toughness of the fresh joints, but it was only marginal. The impact of plasma treatment, however, became more evident once the joints were aged. After one week of aging, the fracture toughness of both untreated and sanded specimens decreased. However, no significant drop was observed for the plasma-treated specimens. This resulted in a G_{IIc} value of 7.8 kJ/m² for plasma-treated specimens, which was at least 15% higher than the untreated and sanded cases. These results

verify that the durability of interface bonding in plasma-treated GFRP is superior to that in the untreated and sand-treated specimens.

[Figure 14 about here.]

Conclusions

The effects of cold plasma treatment factors on the surface characteristics of GFRP were investigated using a central composite design (CCD). The DOE was designed with three main plasma factors, i.e., flow rate (ccm), power (w), and time (s) in five levels each and the surface free energy (SFE) was measured as the dependent response. The experiments revealed a highly nonlinear correlation between the SFE and the process factors. A quadratic model was then built for the prediction of the SFE, and its validity was thoroughly discussed. The model showed great predictability such that the predicted value of 78.63 mW/m at optimized conditions was experimentally measured to be 77.42 mW/m with only a 1.5% difference. The results revealed that, compared to no treatment and sanding, the optimized plasma treatment offers significantly higher SFE values that are primarily composed of polar component. About 99% of the total SFE was polar in the plasma-treated sample, while that was minor in other cases. Further, the fracture experiments of fresh and aged GFRP/adhesive joints proved more stable interfaces in the plasma treated cases, due to the formation of covalent bonds between the adhesive and the functional groups that formed during the plasma treatment. Consequently, the fracture toughness of the plasma-treated specimens did not drop after seawater immersion, while that for the untreated and sand-treated specimen showed about 15% drop. The results of this work reveal the great impact of plasma treatment on the long-term durability of GFRP/adhesive joints, especially exposed to harsh environments such as offshore wind turbines.

Acknowledgment

This work is supported by National Science Foundation Grant No. 1916715, Industry/University

Cooperative Research Center for the Wind Energy Science Technology and Research (I/UCRC WindSTAR).

Any opinions, findings, conclusions, or recommendations expressed in this material are those of the author(s) and do not necessarily reflect the views of the National Science Foundation. The authors would also like to thank

Dr. Ramaswamy Nagarajan and Dr. Amy Peterson for providing access to Benchtop Plasma System and Optical Tensiometer, respectively.

CRediT authorship contribution statement

Nahal Aliheidari: Data curation; Formal analysis; Investigation; Methodology; Writing - original draft; Amir

Ameli: Conceptualization; Formal analysis; Funding acquisition; Methodology; Project administration;

Resources; Supervision; Validation; Writing - review & editing

References

- [1] Ma HL, Jia Z, Lau KT, Leng J, Hui D. Impact properties of glass fiber/epoxy composites at cryogenic environment. Compos Part B Eng 2016;92:210–7. https://doi.org/10.1016/j.compositesb.2016.02.013.
- [2] Thamizh Selvan R, Vishakh Raja PC, Mangal P, Mohan N, Bhowmik S. Recycling technology of epoxy glass fiber and epoxy carbon fiber composites used in aerospace vehicles. J Compos Mater 2021;55:3281–92. https://doi.org/10.1177/00219983211011532.
- [3] Idrisi AH, Mourad AHI, Abdel-Magid BM, Shivamurty B. Investigation on the durability of e-glass/epoxy composite exposed to seawater at elevated temperature. Polymers (Basel) 2021;13. https://doi.org/10.3390/polym13132182.
- [4] Colangelo F, Russo P, Cimino F, Cioffi R, Farina I, Fraternali F, et al. Epoxy/glass fibres composites for civil applications: Comparison between thermal and microwave crosslinking routes. Compos Part B Eng 2017;126:100–7. https://doi.org/10.1016/j.compositesb.2017.06.003.
- [5] Ansal Muhammed K, Ramesh Kannan C, Stalin B, Ravichandran M. Experimental investigation on AW 106 Epoxy/E-Glass fiber/nano clay composite for wind turbine blade. Mater Today Proc 2020;21:202–5. https://doi.org/10.1016/j.matpr.2019.04.221.
- [6] Tserpes K. Adhesive Bonding of Aircraft Structures. Revolutionizing Aircr Mater Process 2020:337–57. https://doi.org/10.1007/978-3-030-35346-9_12.
- [7] Maggiore S, Banea MD, Stagnaro P, Luciano G. A review of structural adhesive joints in hybrid joining processes. Polymers (Basel) 2021;13:3961. https://doi.org/10.3390/polym13223961.
- [8] Baldan A. Adhesion phenomena in bonded joints. Int J Adhes Adhes 2012;38:95-116. https://doi.org/10.1016/j.ijadhadh.2012.04.007.
- [9] Vietri U, Guadagno L, Raimondo M, Vertuccio L, Lafdi K. Nanofilled epoxy adhesive for structural aeronautic materials. Compos Part B Eng 2014;61:73–83. https://doi.org/10.1016/j.compositesb.2014.01.032.
- [10] Wang B, Bai Y, Hu X, Lu P. Enhanced epoxy adhesion between steel plates by surface treatment and CNT/short-fibre reinforcement. Compos Sci Technol 2016;127:149–57. https://doi.org/10.1016/j.compscitech.2016.03.008.
- [11] Anyfantis KN, Tsouvalis NG. The effect of surface preparation on the behaviour of double strap adhesive joints with thick steel adherents. Proc MARSTRUCT 2009, 2nd Int Conf Mar Struct Des Mar Struct 2009:387–92. https://doi.org/10.1201/9780203874981-53.
- [12] van Dam JPB, Abrahami ST, Yilmaz A, Gonzalez-Garcia Y, Terryn H, Mol JMC. Effect of surface roughness and chemistry on the adhesion and durability of a steel-epoxy adhesive interface. Int J Adhes Adhes 2020;96:102450. https://doi.org/10.1016/j.ijadhadh.2019.102450.
- [13] Feng Z, Zhao H, Tan C, Chen J, Wang Y, Chen B, et al. Modification of surface treatment on the strength of 30CrMnSiA steel adhesively bonded joints. Mater Res Express 2019;6:116521. https://doi.org/10.1088/2053-1591/AB4483.
- [14] Kanerva M, Sarlin E, Hoikkanen M, Rämö K, Saarela O, Vuorinen J. Interface modification of glass fibre-polyester composite-composite joints using peel plies. Int J Adhes Adhes 2015;59:40–52. https://doi.org/10.1016/j.ijadhadh.2015.01.016.
- [15] Morano C, Tao R, Alfano M, Lubineau G. Effect of mechanical pretreatments on damage mechanisms and fracture toughness in cfrp/epoxy joints. Materials (Basel) 2021;14:1512. https://doi.org/10.3390/ma14061512.
- [16] Nasreen A, Bangash MK, Shaker K, Nawab Y. Effect of surface treatment on the performance of composite-composite and composite-metal adhesive joints. Polym Compos 2022;43:6320–31. https://doi.org/10.1002/pc.26940.
- $[17]\ Ebnesajjad\ S.\ Material\ Surface\ Preparation\ Techniques.\ Handb\ Adhes\ Surf\ Prep\ Technol\ Appl\ Manuf\ 2010:49-81.$ https://doi.org/10.1016/B978-1-4377-4461-3.10005-7.
- [18] Fabbri P, Messori M. Surface Modification of Polymers: Chemical, Physical, and Biological Routes. Modif Polym Prop 2017:109–30. https://doi.org/10.1016/B978-0-323-44353-1.00005-1.

- [19] Trey SM, Sidenvall P, Alavi K, Ståhlberg D, Johansson M. Dual cure (UV/thermal) primers for composite substrates-Effect of surface treatment and primer composition on adhesion. Prog Org Coatings 2009;64:489–96. https://doi.org/10.1016/j.porgcoat.2008.08.017.
- [20] Chan IM, Cheng WC, Hong FC. Enhanced performance of organic light-emitting devices by atmospheric plasma treatment of indium tin oxide surfaces. Appl Phys Lett 2002;80:13–5. https://doi.org/10.1063/1.1428624.
- [21] Yoshida S, Hagiwara K, Hasebe T, Hotta A. Surface modification of polymers by plasma treatments for the enhancement of biocompatibility and controlled drug release. Surf Coatings Technol 2013;233:99–107. https://doi.org/10.1016/j.surfcoat.2013.02.042.
- [22] Sundriyal P, Pandey M, Bhattacharya S. Plasma-assisted surface alteration of industrial polymers for improved adhesive bonding. Int J Adhes Adhes 2020;101:102626. https://doi.org/10.1016/J.IJADHADH.2020.102626.
- [23] Thompson R, Austin D, Wang C, Neville A, Lin L. Low-frequency plasma activation of nylon 6. Appl Surf Sci 2021;544:148929. https://doi.org/10.1016/j.apsusc.2021.148929.
- [24] Birer Ö. Reactivity zones around an atmospheric pressure plasma jet. Appl Surf Sci 2015;354:420–8. https://doi.org/10.1016/j.apsusc.2015.04.100.
- [25] Kantharaju S, Vinodhini J, Govindaraju M, Bhowmik S. An investigation to enhance the mechanical property of high-performance thermoplastic composite through different plasma treatment. Polym Compos 2023;44:178–89. https://doi.org/10.1002/pc.27037.
- [26] Zhang S, Awaja F, James N, McKenzie DR, Ruys AJ. Autohesion of plasma treated semi-crystalline PEEK: Comparative study of argon, nitrogen and oxygen treatments. Colloids Surfaces A Physicochem Eng Asp 2011;374:88–95. https://doi.org/10.1016/j.colsurfa.2010.11.013.
- [27] Bagiatis V, Critchlow GW, Price D, Wang S. The effect of atmospheric pressure plasma treatment (APPT) on the adhesive bonding of poly(methyl methacrylate) (PMMA)-to-glass using a polydimethylsiloxane (PDMS)-based adhesive. Int J Adhes Adhes 2019;95:102405. https://doi.org/10.1016/j.ijadhadh.2019.102405.
- [28] Hassan EAM, Yang L, Elagib THH, Ge D, Lv X, Zhou J, et al. Synergistic effect of hydrogen bonding and π - π stacking in interface of CF/PEEK composites. Compos Part B Eng 2019;171:70–7. https://doi.org/10.1016/j.compositesb.2019.04.015.
- [29] Lee H, Ohsawa I, Takahashi J. Effect of plasma surface treatment of recycled carbon fiber on carbon fiber-reinforced plastics (CFRP) interfacial properties. Appl Surf Sci 2015;328:241–6. https://doi.org/10.1016/j.apsusc.2014.12.012.
- [30] Encinas N, Lavat-Gil M, Dillingham RG, Abenojar J, Martínez MA. Cold plasma effect on short glass fibre reinforced composites adhesion properties. Int J Adhes Adhes 2014;48:85–91. https://doi.org/10.1016/j.ijadhadh.2013.09.026.
- [31] Heidemann HM, Dotto MER, Laurindo JB, Carciofi BAM, Costa C. Cold plasma treatment to improve the adhesion of cassava starch films onto PCL and PLA surface. Colloids Surfaces A Physicochem Eng Asp 2019;580:123739. https://doi.org/10.1016/j.colsurfa.2019.123739.
- [32] Baghery Borooj M, Mousavi Shoushtari A, Haji A, Nosratian Sabet E. Optimization of plasma treatment variables for the improvement of carbon fibres/epoxy composite performance by response surface methodology. Compos Sci Technol 2016;128:215–21. https://doi.org/10.1016/j.compscitech.2016.03.020.
- [33] Cho BG, Hwang SH, Park M, Park JK, Park Y Bin, Chae HG. The effects of plasma surface treatment on the mechanical properties of polycarbonate/carbon nanotube/carbon fiber composites. Compos Part B Eng 2019;160:436–45. https://doi.org/10.1016/j.compositesb.2018.12.062.
- [34] Unterweger C, Duchoslav J, Stifter D, Fürst C. Characterization of carbon fiber surfaces and their impact on the mechanical properties of short carbon fiber reinforced polypropylene composites. Compos Sci Technol 2015;108:41–7. https://doi.org/10.1016/j.compscitech.2015.01.004.
- [35] Haji, A., Hadizadeh, M., Ferasat, E., & Movaghatian, D. Effect of Plasma Treatment on Glass Fiber/Epoxy Resin Composite. In Proceedings of the 2nd International Congress of Innovative Textiles Çorlu, Turkey 2019: 17-18.
- [36] Dighton C, Rezai A, Ogin SL, Watts JF. Atmospheric plasma treatment of CFRP composites to enhance structural bonding investigated using surface analytical techniques. Int J Adhes Adhes 2019;91:142–9. https://doi.org/10.1016/J.IJADHADH.2019.03.010.
- [37] Gude MR, Prolongo SG, Ureña A. Adhesive bonding of carbon fibre/epoxy laminates: Correlation between surface and mechanical properties. Surf Coatings Technol 2012;207:602–7. https://doi.org/10.1016/j.surfcoat.2012.07.085.
- [38] Wang D, Li Y, Zou T, Fu J, Liu Z. Increasing strength and fracture toughness of carbon fibre-reinforced plastic adhesively bonded joints by combining peel-ply and oxygen plasma treatments. Appl Surf Sci 2023;612:155768. https://doi.org/10.1016/j.apsusc.2022.155768.

- [39] Karimifard S, Alavi Moghaddam MR. Application of response surface methodology in physicochemical removal of dyes from wastewater: A critical review. Sci Total Environ 2018;640–641:772–97. https://doi.org/10.1016/j.scitotenv.2018.05.355.
- [40] Srivastava M, Maheshwari S, Kundra T, Rathee S. Multi-Response Optimization of Fused Deposition Modelling Process Parameters of ABS Using Response Surface Methodology (RSM)-Based Desirability Analysis. Mater. Today Proc., vol. 4, Elsevier Ltd; 2017, p. 1972–7. https://doi.org/10.1016/j.matpr.2017.02.043.
- [41] Chelladurai SJS, Murugan K, Ray AP, Upadhyaya M, Narasimharaj V, Gnanasekaran S. Optimization of process parameters using response surface methodology: A review. Mater Today Proc 2020;37:1301–4. https://doi.org/10.1016/j.matpr.2020.06.466.
- [42] Jankovic A, Chaudhary G, Goia F. Designing the design of experiments (DOE) An investigation on the influence of different factorial designs on the characterization of complex systems. Energy Build 2021;250:111298. https://doi.org/10.1016/j.enbuild.2021.111298.
- [43] Zhou L, Yan G, Ou J. Response Surface Method Based on Radial Basis Functions for Modeling Large-Scale Structures in Model Updating. Comput Civ Infrastruct Eng 2013;28:210–26. https://doi.org/10.1111/j.1467-8667.2012.00803.x.
- [44] Zenkiewicz M. Comparative study on the surface free energy of a solid calculated by different methods. Polym Test 2007;26:14–9. https://doi.org/10.1016/j.polymertesting.2006.08.005.
- [45] Awaja F, Gilbert M, Kelly G, Fox B, Pigram PJ. Adhesion of polymers. Prog Polym Sci 2009;34:948–68. https://doi.org/10.1016/j.progpolymsci.2009.04.007.
- [46] Stammitti-Scarpone A, Acosta EJ. Solid-liquid-liquid wettability and its prediction with surface free energy models. Adv Colloid Interface Sci 2019;264:28–46. https://doi.org/10.1016/j.cis.2018.10.003.
- [47] Şenay V, Özen S, Pat S, Korkmaz Ş. A study on some physical properties of a Pb-doped GaAs thin film produced by thermionic vacuum arc. J Alloys Compd 2017;720:383–7. https://doi.org/10.1016/j.jallcom.2017.05.297.
- [48] Rudawska A. The effect of the salt water aging on the mechanical properties of epoxy adhesives compounds. Polymers (Basel) 2020;12:843. https://doi.org/10.3390/POLYM12040843.
- [49] Ameli A, Datla N V., Azari S, Papini M, Spelt JK. Prediction of environmental degradation of closed adhesive joints using data from open-faced specimens. Compos Struct 2012;94:779–86. https://doi.org/10.1016/j.compstruct.2011.09.017.
- [50] ASTM D7905. Standard test method for determination of the mode II interlaminar fracture toughness of unidirectional fiber-reinforced polymer matrix composites. Astm 2014:1–18. https://doi.org/10.1520/D7905_D7905M-19E01
- [51] Shmueli G. To explain or to predict? Stat Sci 2010;25:289-310. https://doi.org/10.1214/10-STS330.
- [52] Bashir MJK, Aziz HA, Yusoff MS, Adlan MN. Application of response surface methodology (RSM) for optimization of ammoniacal nitrogen removal from semi-aerobic landfill leachate using ion exchange resin. Desalination 2010;254:154–61. https://doi.org/10.1016/j.desal.2009.12.002.
- [53] Darvishmotevalli M, Zarei A, Moradnia M, Noorisepehr M, Mohammadi H. Optimization of saline wastewater treatment using electrochemical oxidation process: Prediction by RSM method. MethodsX 2019;6:1101–13. https://doi.org/10.1016/j.mex.2019.03.015.
- [54] Şimşek B, İç YT, Şimşek EH. A RSM-Based Multi-Response Optimization Application for Determining Optimal Mix Proportions of Standard Ready-Mixed Concrete. Arab J Sci Eng 2016;41:1435–50. https://doi.org/10.1007/s13369-015-1987-0.
- [55] Perec A. Multiple response optimization of abrasive water jet cutting process using Response Surface Methodology (RSM). Procedia Comput Sci 2021;192:931–40. https://doi.org/10.1016/j.procs.2021.08.096.
- [56] Lavery MR, Acharya P, Sivo SA, Xu L. Number of predictors and multicollinearity: What are their effects on error and bias in regression? Commun Stat Simul Comput 2019;48:27–38. https://doi.org/10.1080/03610918.2017.1371750.
- [57] O'Brien RM. A caution regarding rules of thumb for variance inflation factors. Qual Quant 2007;41:673–90. https://doi.org/10.1007/s11135-006-9018-6.
- [58] Flaifel MH. An approach towards optimization appraisal of thermal conductivity of magnetic thermoplastic elastomeric nanocomposites using response surface methodology. Polymers (Basel) 2020;12:2030. https://doi.org/10.3390/POLYM12092030.
- [59] Zaldivar RJ, Steckel GL, Morgan BA, Nokes JP, Kim HI. Bonding optimization on composite surfaces using atmospheric plasma treatment. J Adhes Sci Technol 2012;26:381–401. https://doi.org/10.1163/016942411X576554.
- [60] Lim KB, Lee BS, Kim JT, Lee DC. Correlation of surface hydrophilicity and surface static properties in epoxy/glass fibre after plasma treatment. Surf Interface Anal 2002;33:918–23. https://doi.org/10.1002/SIA.1445.
- [61] Pitchan MK, Bhowmik S, Balachandran M, Abraham M. Process optimization of functionalized MWCNT/polyetherimide nanocomposites for aerospace application. Mater Des 2017;127:193–203. https://doi.org/10.1016/j.matdes.2017.04.081.

- [62] Del Castillo E, Montgomery DC, McCarville DR. Modified desirability functions for multiple response optimization. J Qual Technol 1996;28:337–45. https://doi.org/10.1080/00224065.1996.11979684.
- [63] Yang G, Yang T, Yuan W, Du Y. The influence of surface treatment on the tensile properties of carbon fiber-reinforced epoxy composites-bonded joints. Compos Part B Eng 2019;160:446–56. https://doi.org/10.1016/j.compositesb.2018.12.095.
- [64] Yudhanto A, Alfano M, Lubineau G. Surface preparation strategies in secondary bonded thermoset-based composite materials: A review. Compos Part A Appl Sci Manuf 2021;147:106443. https://doi.org/10.1016/j.compositesa.2021.106443.
- [65] Pornwannachai W, Richard Horrocks A, Kandola BK. Surface Modification of Commingled Flax/PP and Flax/PLA Fibres by Silane or Atmospheric Argon Plasma Exposure to Improve Fibre–Matrix Adhesion in Composites. Fibers 2022;10:2. https://doi.org/10.3390/fib10010002.
- [66] Saba N, Jawaid M, Alothman OY, Paridah MT, Hassan A. Recent advances in epoxy resin, natural fiber-reinforced epoxy composites and their applications. J Reinf Plast Compos 2016;35:447–70. https://doi.org/10.1177/0731684415618459.
- [67] Kim DK, Choi YH, Kim KW, Kim BJ. Transparent glass-fiber-reinforced epoxy composites and their optical characteristics. Compos Sci Technol 2023;232:109848. https://doi.org/10.1016/j.compscitech.2022.109848.
- [68] Dai J, Liu XH, Xiao YJ, Yang JH, Qi PK, Wang J, et al. High hydrophilicity and excellent adsorption ability of a stretched polypropylene/graphene oxide composite membrane achieved by plasma assisted surface modification. RSC Adv 2015;5:71240–52. https://doi.org/10.1039/c5ra10310j.
- [69] Dimitrakellis P, Faubert F, Wartel M, Gogolides E, Pellerin S. Plasma Surface Modification of Epoxy Polymer in Air DBD and Gliding Arc. Processes 2022;10:104. https://doi.org/10.3390/pr10010104.
- [70] Anbumani S, da Silva AM, Roggero UFS, Silva AMPA, Hernández-Figueroa HE, Cotta MA. Oxygen plasma-enhanced covalent biomolecule immobilization on SU-8 thin films: A stable and homogenous surface biofunctionalization strategy. Appl Surf Sci 2021;553:149502. https://doi.org/10.1016/j.apsusc.2021.149502.
- [71] Xu LY, Lu JR, Li KM, Hu J. Experimental study of CFRP laser surface modification and bonding characteristics of CFRP/Al6061 heterogeneous joints. Compos Struct 2022;283:115030. https://doi.org/10.1016/j.compstruct.2021.115030.
- [72] Cvelbar U, Pejovnik S, Mozetiè M, Zalar A. Increased surface roughness by oxygen plasma treatment of graphite/polymer composite. Appl Surf Sci 2003;210:255–61. https://doi.org/10.1016/S0169-4332(02)01286-2.
- [73] Garpelli FP, González Ramírez FM, Sales R de CM, Arbelo MA, Shiino MY, Resende HB, et al. Experimental characterization of Mode II fatigue delamination growth onset in composite Joints. J Compos Mater 2022;56:115–32. https://doi.org/10.1177/00219983211056736.

List of Figures

FIGURE 1. SURFACE TREATMENT METHODS. 25
FIGURE 2. SCHEMATIC DIAGRAM OF THE SURFACE MODIFICATION PROCESS USING RADIOFREQUENCY COLD
PLASMA
FIGURE 3 (A) SCHEMATIC OF MODIFIED ASTM D-7905 AND JOINT FABRICATION LAYUP (B) MAGNIFIED JOINT
CROSS SECTION (C) FRACTURE TEST SETUP26
FIGURE 4. (A) NORMAL PROBABILITY PLOT WHERE THE SFE IS THE RESPONSE, (B) THE HISTOGRAM AND FITTED
NORMAL DISTRIBUTION OF THE SFE, AND (C) THE QUANTILE-QUANTILE $(Q-Q)$ PLOT OF THE NORMAL
DISTRIBUTION
FIGURE 5. PARETO CHART OF THE MAIN FACTORS AND THEIR INTERACTIONS. SFE IS THE RESPONSE. F, T, AND P
DENOTE THE FLOW RATE, TIME, AND POWER, RESPECTIVELY27
FIGURE 6. THE DEPENDENCE OF SFE ON (A) MAIN EFFECTS OF TIME, POWER, AND FLOW RATE, AND (B) TIME AND
POWER INTERACTION27
FIGURE 7. RSM 2D CONTOUR PLOTS FOR THE RESPONSE: (A) POWER VS. TIME, (B) FLOW RATE VS. TIME, AND (C)
FLOW RATE VS. POWER28
FIGURE 8. THE SURFACE FREE ENERGY OF THE GFRP SAMPLES SANDED WITH DIFFERENT GRIT NUMBERS28
FIGURE 9, COMPARISON OF (A) CONTACT ANGLES, AND (B) SURFACE FREE ENERGIES OF UNTREATED, SANDED, AND

PLASMA-TREATED GFRP SAMPLES.	29
FIGURE 10. ATR-FTIR SPECTRA OF GFRP, FROM TOP TO BOTTOM: UNTREATED (BLUE), SANDED (RED), AND	
PLASMA-TREATED (GREEN) GFRP SAMPLES.	29
FIGURE 11. THE SURFACE TOPOLOGY OF (A) UNTREATED, (B) SANDED, AND (C) PLASMA-TREATED GFRP SAMPLE	S.
	30
FIGURE 12. SEM MICROGRAPHS OF (A AND D) UNTREATED, (B AND E) SANDED, AND (C AND F) PLASMA-TREATED	
GFRP SAMPLES AT DIFFERENT MAGNIFICATIONS OF (50 AND 1500)	30
FIGURE 13. THE FRACTURE SURFACE IMAGES TAKEN FROM THE UPPER SIDE ADHEREND OF AGED JOINTS: (A)	
UNTREATED, (B) SANDED, AND (C) PLASMA-TREATED GFRP SURFACE. THE DASHED ARROWS SHOW THE	
CRACK ADVANCE DIRECTION.	31
FIGURE 14. (A) THE REPRESENTATIVE LOAD-DISPLACEMENT CURVES AND (B) THE AVERAGE FRACTURE	
TOUGHNESS OF FRESH AND AGED JOINTS WITH UNTREATED, SAND-TREATED, AND PLASMA-TREATED JOINTS	
	31
List of Tables	
List of Tables	
TABLE 1: PLASMA PROCESS FACTORS AND THEIR ACTUAL AND CODED LEVELS UTILIZED IN THE CENTRAL	
COMPOSITE DESIGN (CCD).	32
TABLE 2: THE RANDOMIZED DESIGN OF EXPERIMENT (DOE) MATRIX WITH ACTUAL AND CODED VALUES OF THE	52
PROCESS FACTORS ALONG WITH THE MEASURED SURFACE FREE ENERGY (SFE) AS THE OUTPUT RESPONSE	32
TABLE 3: THE POLAR AND DISPERSIVE SURFACE ENERGY COMPONENTS OF THE LIQUIDS USED FOR CONTACT ANG	
MEASUREMENTS.	
TABLE 4: ANALYSIS OF VARIANCE (ANOVA) FOR SFE RESPONSE WITH TIME, POWER, AND FLOWRATE AS THE	
	33
PROCESS FACTORS	
	34

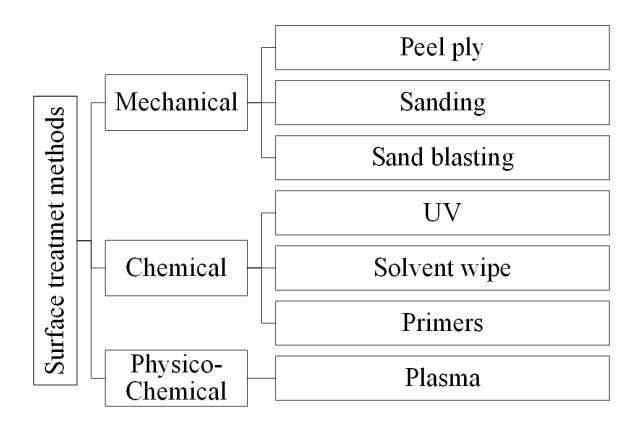


Figure 1. Surface treatment methods.

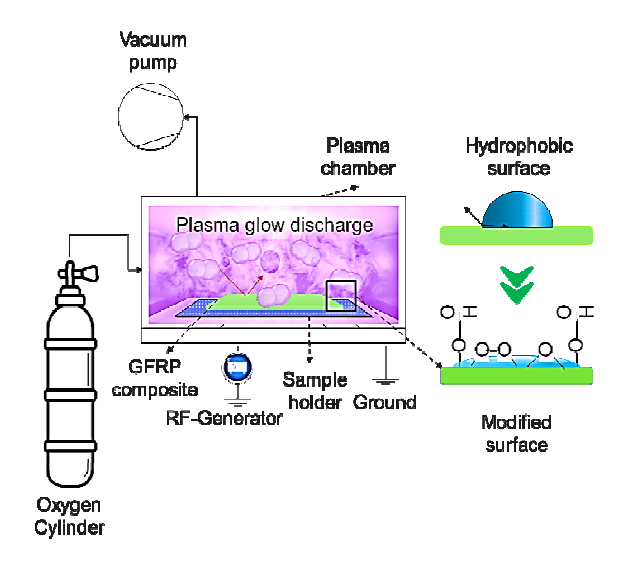


Figure 2. Schematic diagram of the surface modification process using radiofrequency cold plasma.

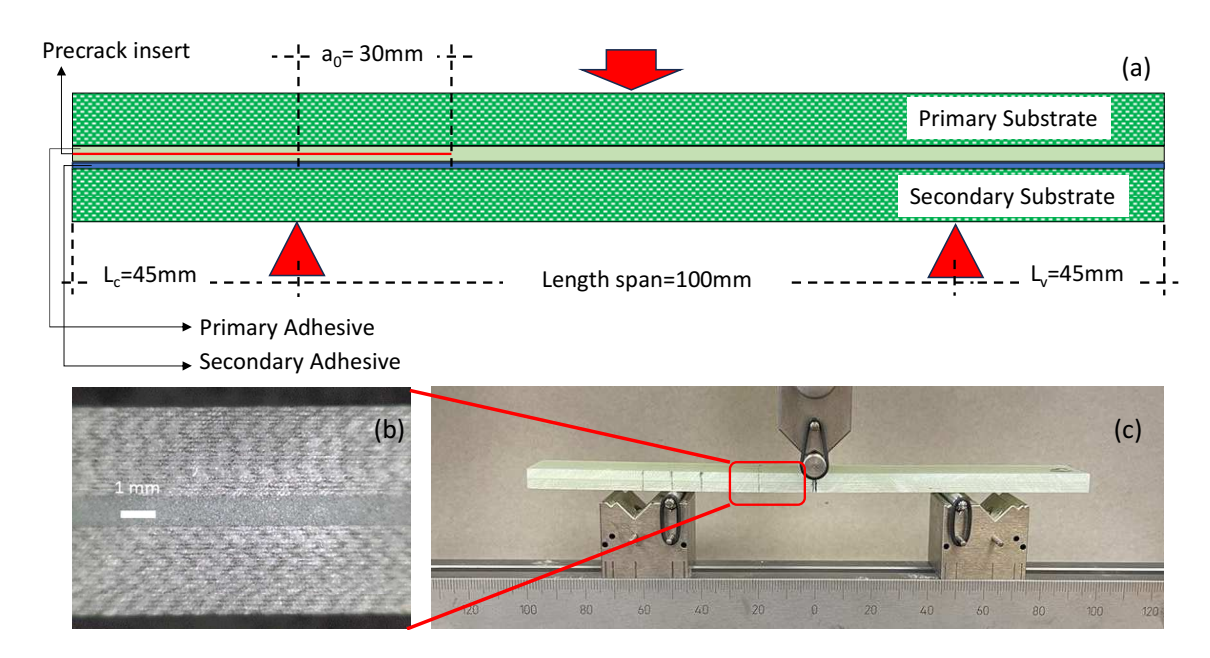


Figure 3 (a) Schematic of modified ASTM D-7905 ENF specimen, (b) magnified side view of ENF Specimen, and (c) ENF fracture test setup.

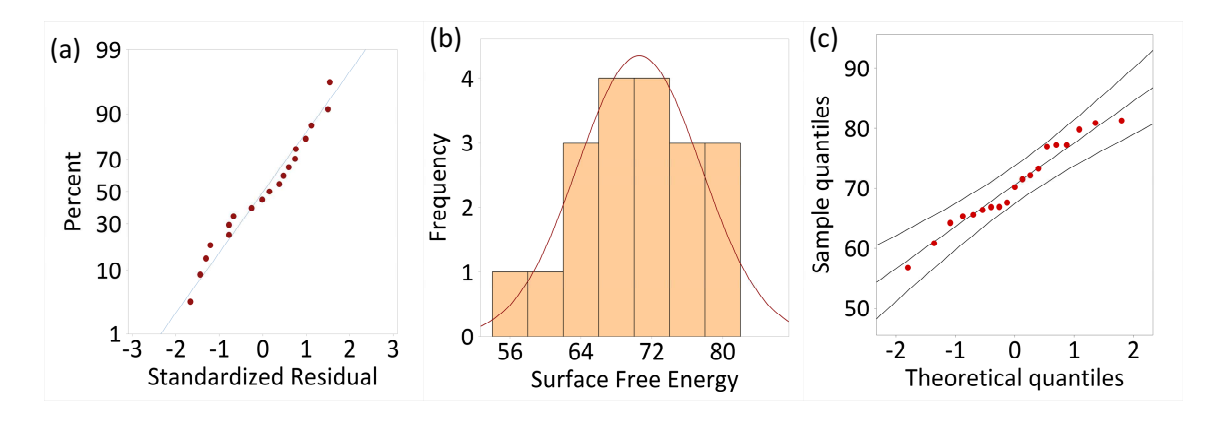


Figure 4. (a) Normal probability plot where the SFE is the response, (b) The histogram and fitted normal distribution of the SFE, and (c) the quantile-quantile (Q-Q) plot of the normal distribution.

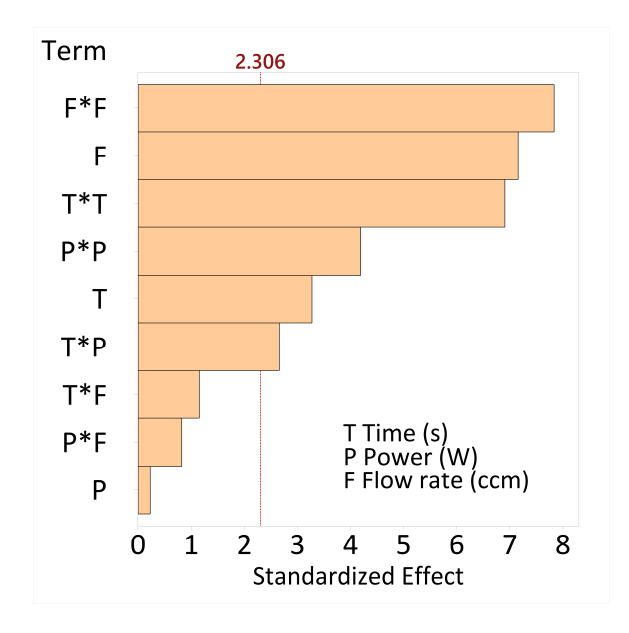


Figure 5. Pareto chart of the main factors and their interactions. SFE is the response. F, T, and P denote the flow rate, time, and power, respectively.

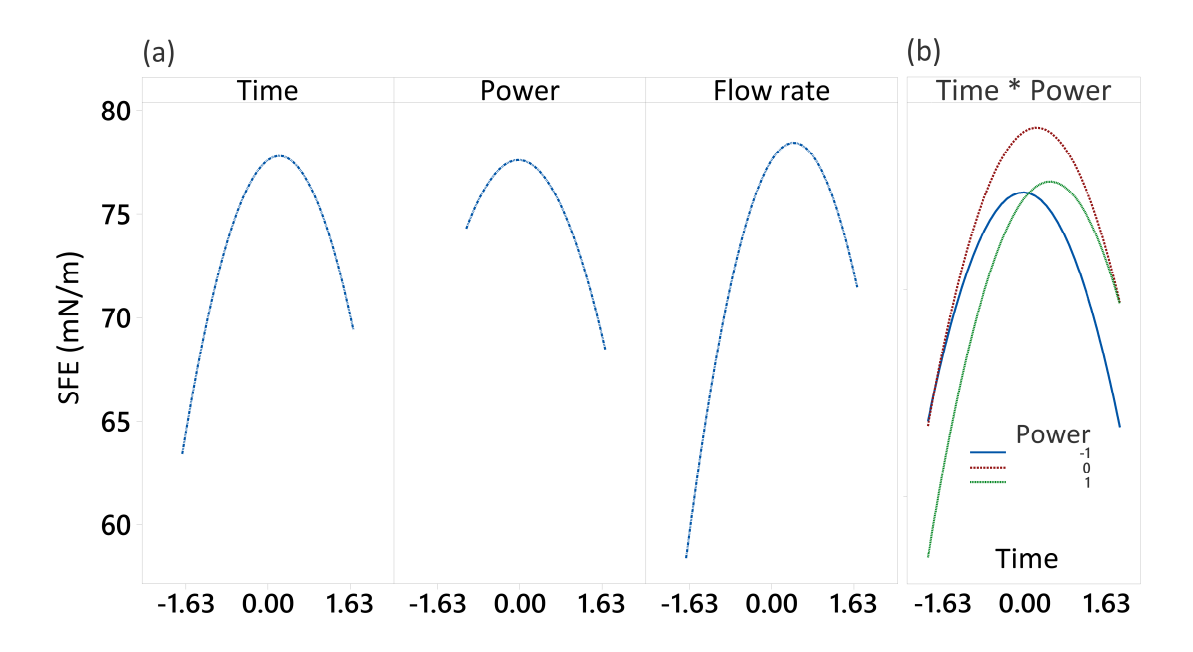


Figure 6. The dependence of SFE on (a) main effects of Time, Power, and Flow Rate, and (b) Time and Power interaction, based on the final reduced quadratic model.

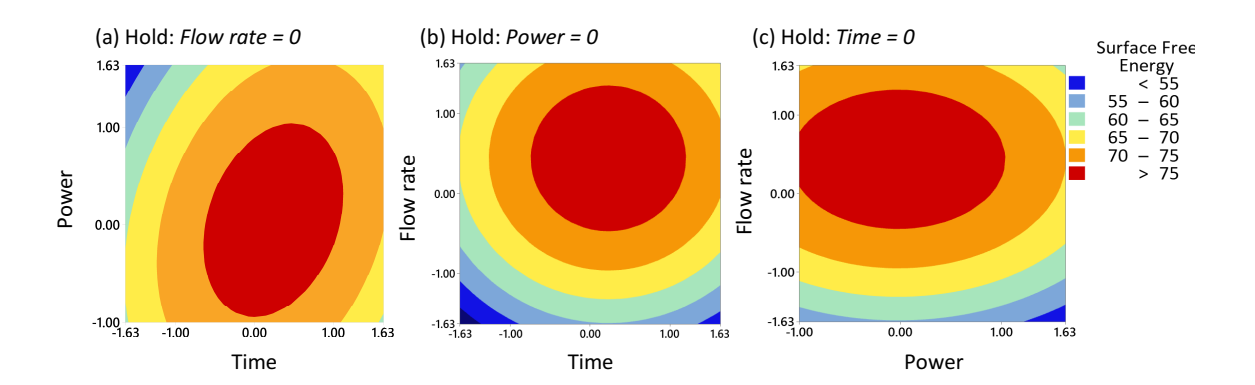


Figure 7. RSM 2D contour plots for the response: (a) Power vs. Time, (b) Flow rate vs. Time, and (c) Flow Rate vs. Power.

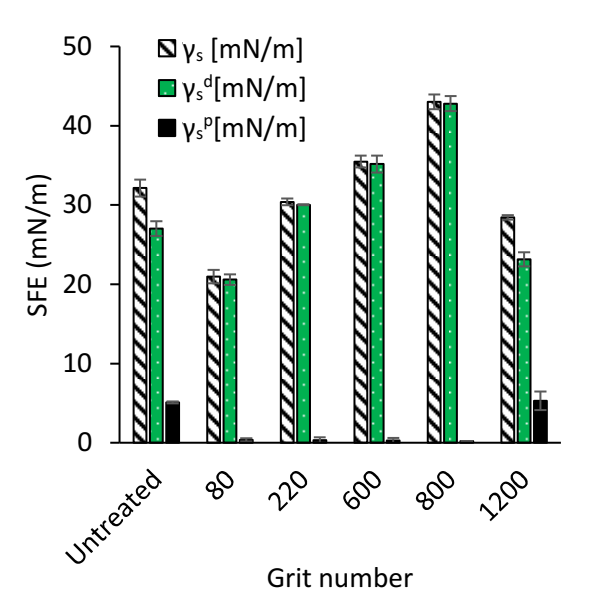


Figure 8. The surface free energy of the GFRP samples sanded with different grit numbers.

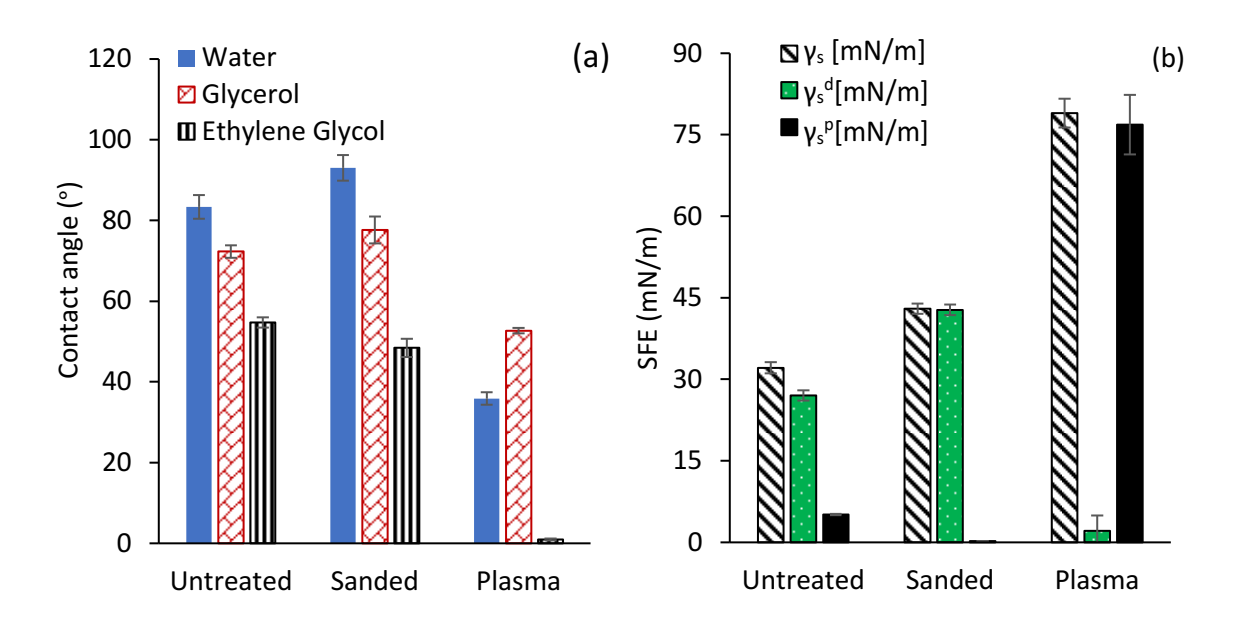


Figure 9. Comparison of (a) contact angles, and (b) surface free energies of untreated, sanded, and plasma-treated GFRP samples.

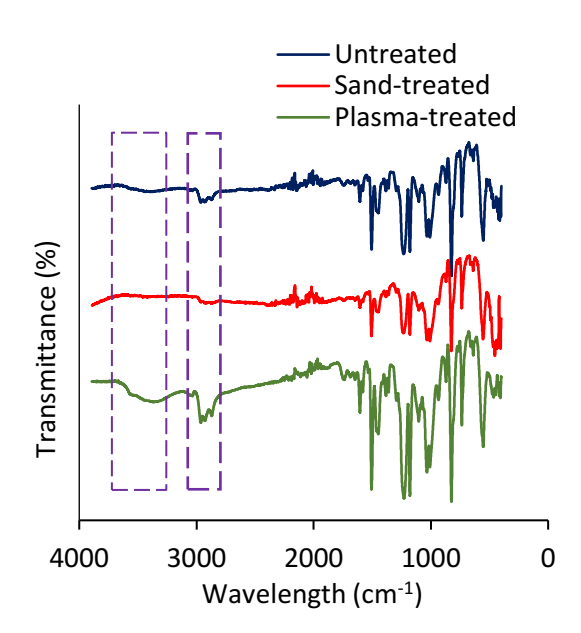
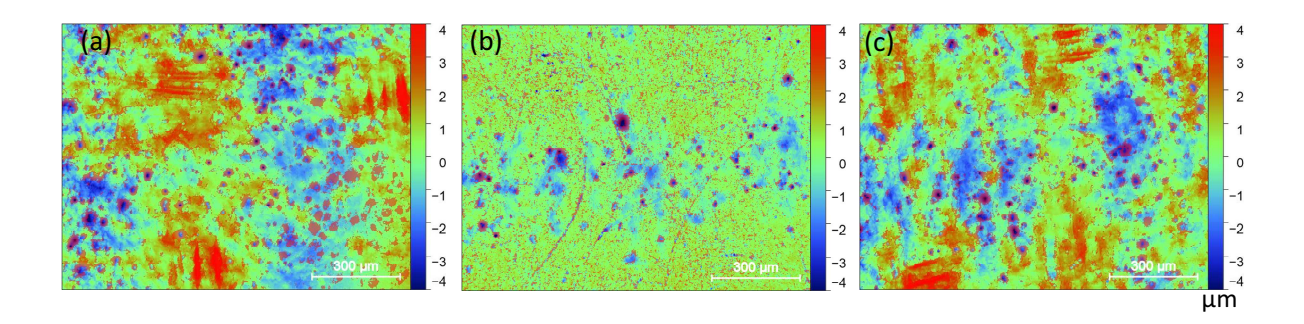


Figure 10. ATR-FTIR spectra of GFRP, from top to bottom: untreated (Blue), sanded (Red), and plasma-treated (Green) GFRP samples.



 $Figure\ 11.\ The\ surface\ topology\ of\ (a)\ untreated, (b)\ sanded,\ and\ (c)\ plasma-treated\ GFRP\ samples.$

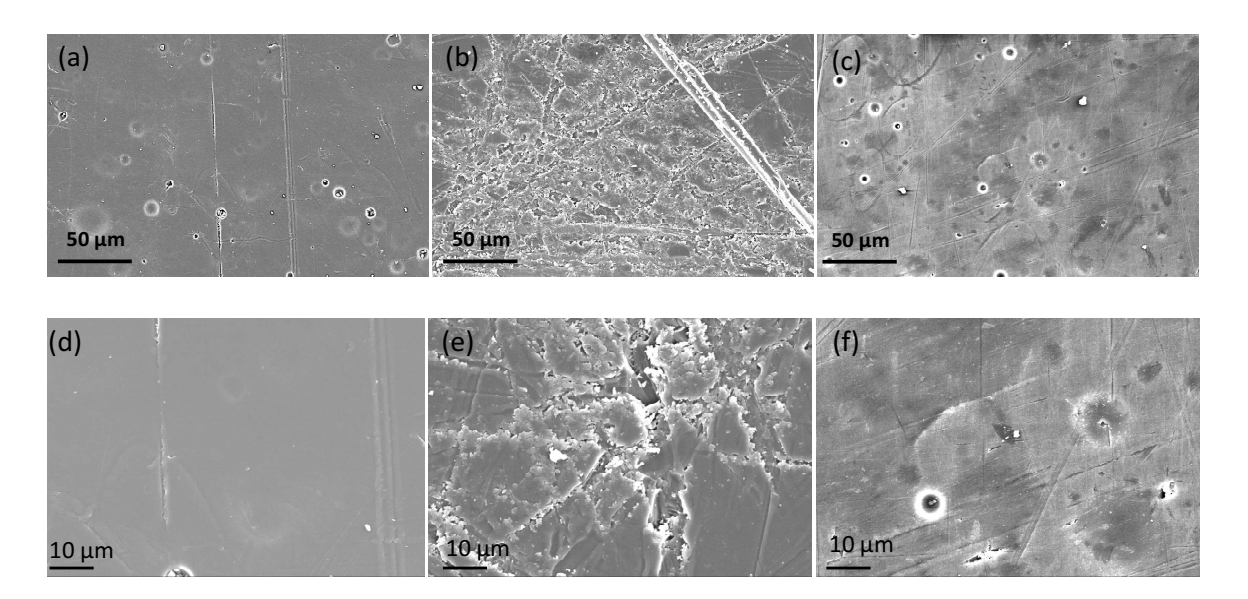


Figure 12. SEM micrographs of (a and d) untreated, (b and e) sanded, and (c and f) plasma-treated GFRP samples at different magnifications of (50 and 1500).

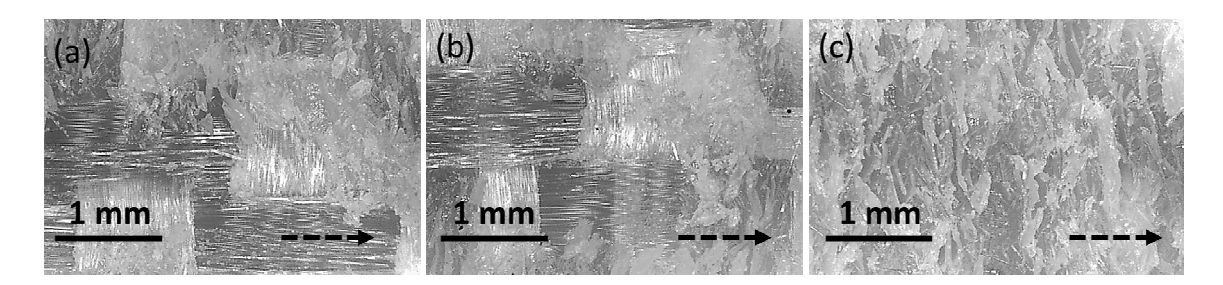


Figure 13. The fracture surface images taken from the upper side adherend of aged joints: (a) untreated, (b) sanded, and (c) plasma-treated GFRP surface. The dashed arrows show the crack advance direction.

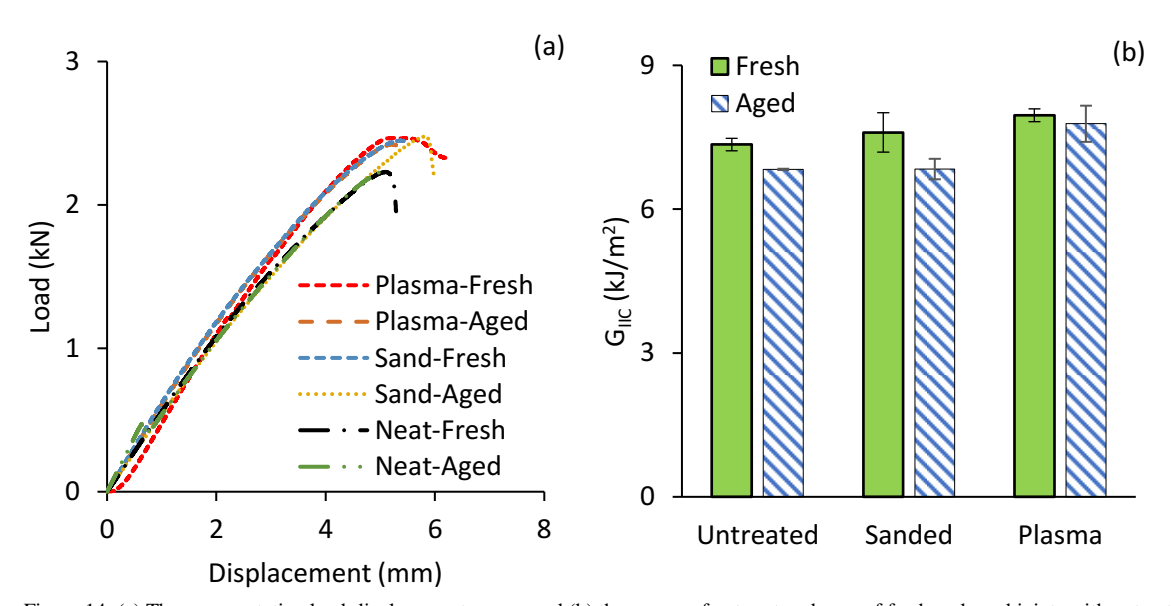


Figure 14. (a) The representative load-displacement curves and (b) the average fracture toughness of fresh and aged joints with untreated, sand-treated, and plasma-treated joints.

Table 1: Plasma process factors and their actual and coded levels utilized in the Central Composite Design (CCD).

Levels	-1.63	-1	0	1	1.63
Time (s)	10	37	55	82	100
Power (W)	25	78	112	166	200
Flow rate (ccm)	10	22	30	42	50

Table 2: The randomized design of experiment (DOE) matrix with actual and coded values of the process factors along with the measured surface free energy (SFE) as the output response.

Input process factors							Observed response	
		Time,	T(s)	Powe	r, P (W)	Flow ra	te, F (ccm)	SFE (mN/m)
		Coded	Actual	Coded	Actual	Coded	Actual	_
No.	Block							
1	1	0	55	0	112	0	30	81.3
2	1	-1	37	-1	78	1	42	70.2
3	1	0	55	0	112	0	30	77.3
4	1	0	55	0	112	0	30	79.8
5	1	1	82	-1	78	1	42	72.1
6	1	1	82	1	166	1	42	77.3
7	1	0	55	0	112	0	30	80.8
8	1	-1	37	-1	78	-1	22	65.3
9	1	-1	37	1	166	1	42	66.4
10	1	1	82	1	166	-1	22	66.9
11	1	1	82	-1	78	-1	22	65.6
12	1	-1	37	1	166	-1	22	60.8
13	2	-1.63	10	0	112	0	30	64.2
14	2	0	55	0	112	-1.63	10	56.8
15	2	0	55	0	112	0	30	73.2
16	2	0	55	-1.63	25	0	30	*
17	2	1.63	100	0	112	0	30	66.9
18	2	0	55	0	112	1.63	50	71.5
19	2	0	55	1.63	200	0	30	67.6
20	2	0	55	0	112	0	30	76.9

^{*} Successful trial was not possible in this condition, due to a very low power requirement under which the plasma machine did not reliably operate.

Table 3: The polar and dispersive surface energy components of the liquids used for contact angle measurements.

	$\gamma_l (mN/m)$	$\gamma_l^p (mN/m)$	$\gamma_l^d (mN/m)$
Water (W)	72.8	51.0	21.8
Ethylene glycol (EG)	48.0	19.0	29.0
Glycerol (G)	64.0	30.0	34.0

Table 4: Analysis of Variance (ANOVA) for SFE response with time, power, and flowrate as the process factors.

Source	Degree of Freedom (DF)	Sum of Squares (SS)	F-Value	<i>p</i> -Value	Variance Inflation Factor
	, ,	• , ,			(VIF)
Model	8	837.97	27.11	0.0000083	
Linear	3	239.78	20.64	0.0001323	
Time	1	41.38	10.71	0.0083918	1.00
Power	1	0.75	0.05	0.8239324	1.27
Flow rate	1	197.65	51.15	0.0000310	1.00
Square	3	506.48	43.69	0.0000047	
Time*Time	1	164.08	47.63	0.0000419	1.05
Power*Power	1	105.65	17.54	0.0018645	1.27
Flow rate*Flow rate	1	236.75	61.27	0.0000142	1.05
2-Way Interaction	1	27.27	7.06	0.0240388	
Time*Power	1	27.27	7.06	0.0240388	1.00
Error	10	38.64			
Lack-of-Fit	6	22.01	0.88	0.5764518	
Pure Error	4	16.63			
Total	18	876.61			

Table 5: The first three optimized solutions with their SFE and desirability values.

Solution	Time (s)	Power (W)	Flow rate (cc)	SFE Optimization (mN/m)	SFE Experiment (mN/m)	Desirability
1	64	118	36	78.65	77.42	0.89
2	81	165	38	75.01	72.80	0.74
3	77	90	42	74.92	73.52	0.74

Table 6: Surface roughness values for untreated, sanded, and plasma-treated samples.

	S_a	Sz	S_{q}
Untreated	0.896±0.054	13.091±4.362	13.091±0.059
Sand-treated	0.424±0.067	8.110±1.213	0.553±0.806
Plasma-treated	0.892±0.015	12.208±1.741	11.131±0.015